




Research Article


Graphene-based strain sensing in composites for structural and health monitoring applications



Akram Zitoun¹  · Dimitrios Fakis¹ · Nithin Jayasree¹ · Sadik Omairey¹ · Fokion Oikonomidis² · Zlatka Stoeva³ · Mihalis Kazilas^{1,2}

Received: 22 October 2021 / Accepted: 10 January 2022

Published online: 24 January 2022

© The Author(s) 2022 

Abstract

Composite structures are attracting more interest due to their outstanding mechanical properties; thus, their inspection and health assessment are key items for their safe use. In this article we present a graphene-based sensor that evaluates the strain generated within a composite. A finite element model was developed to investigate the mechanism driving the graphene to act as a strain sensor. A prototype sensor was manufactured, using a commercially available graphene ink. The strain in composite samples was measured and the gauge factor identified by applying different load scenarios. The graphene sensor proved to be able to evaluate strain at various levels providing a gauge factor (exceeding 6) higher than commercially available strain gauges.

Article Highlights

- Graphene ink can be used to design and develop strain sensing systems
- Graphene strain sensors are printed directly on the material allowing great design flexibility. The sensors can either be applied on the surface of the composite material or embedded within the structure.
- The measured gauge factor for the graphene strain sensor is higher than the commercial strain sensors.
- The graphene strain sensors provided higher sensing capabilities compared to commercially available copper-based strain gauges.
- The graphene sensor showed consistent results for different mechanical testing scenarios.

✉ Akram Zitoun, akram.zitoun@brunel.ac.uk; Dimitrios Fakis, Dimitrios.Fakis@brunel.ac.uk; Nithin Jayasree, Nithin.Jayasree@brunel.ac.uk; Sadik Omairey, Sadik.Omairey@brunel.ac.uk; Fokion Oikonomidis, fokion.oikonomidis@twi.co.uk; Zlatka Stoeva, zlatka.stoeva@dzptechnologies.com; Mihalis Kazilas, Mihalis.Kazilas@brunel.ac.uk | ¹Brunel Composites Centre, College of Engineering, Design and Physical Sciences, Brunel University London, London UB8 3PH, UK. ²TWI Ltd, Granta Park, Great Abington, Cambridge CB21 6AL, UK. ³Future Business Centre, DZP Technologies Limited, Kings Hedges Road, Cambridge CB4 2HY, UK.



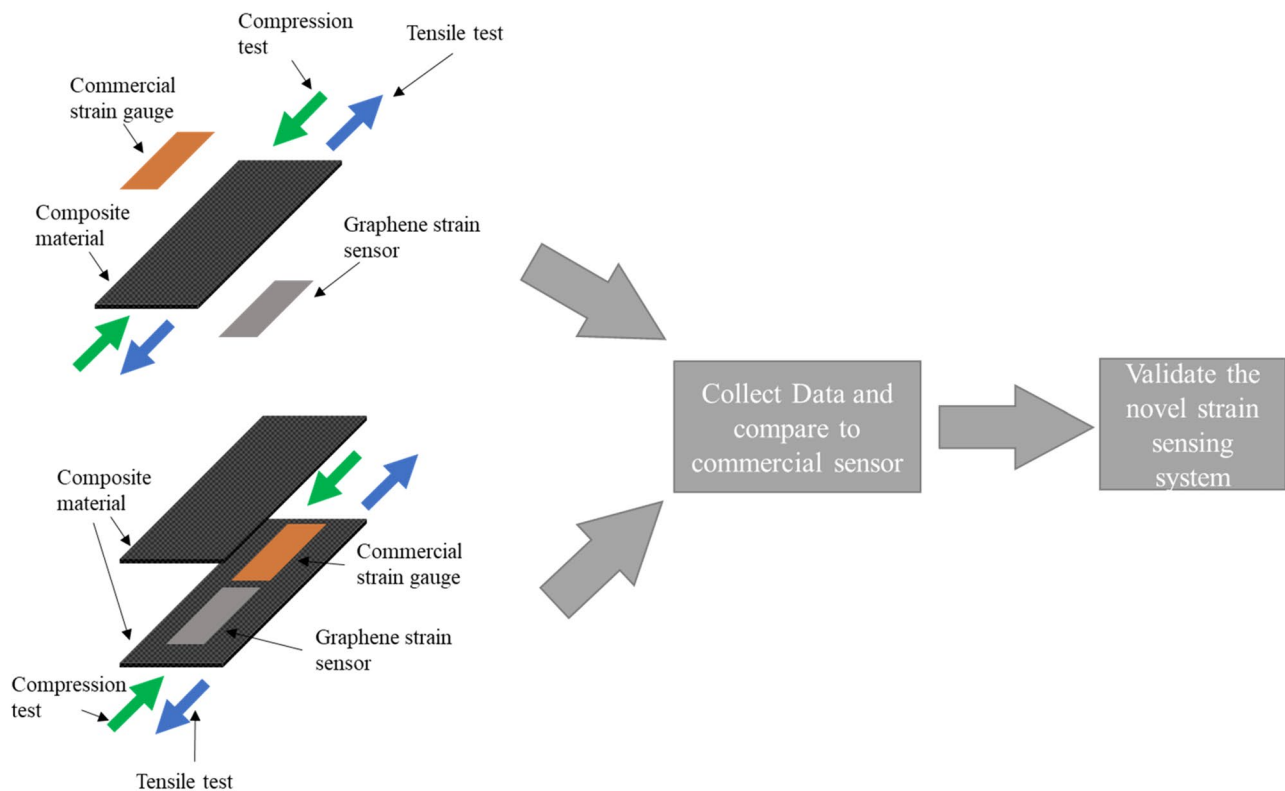
SN Applied Sciences

(2022) 4:58

| <https://doi.org/10.1007/s42452-022-04940-1>

SN Applied Sciences
A **SPRINGER NATURE** journal

Graphical abstract



Keywords Graphene strain sensors · Composite materials · Structural and health monitoring · Graphene sensors

1 Introduction

Structural composite materials in sectors such as aerospace, automotive or renewable energy have significantly increased over the past decades, replacing traditional metals due to their superior mechanical properties, including high specific modulus [1, 2]. The superior properties are established by tailoring the composite layout using appropriate resin matrix systems, combined with layered fibre reinforcement in different stack configurations and orientations to achieve the required mechanical properties [3, 4]. Due to their complex nature, composites are subject to different failure types such as delamination, fibre breakage or cracks in the resin matrix [5, 6]. These damages occur due to numerous factors such as overloading, cyclic loading, impact damage or degradation due to environmental conditions. They can lead to sudden failure or unplanned maintenance if the defect is detected well in advance [7].

When present in the composite, flaws can compromise the mechanical strength and structural integrity of the structure leading to catastrophic failures [8]. To avoid such situations, Non-Destructive Testing (NDT) procedures and

Structural Health Monitoring (SHM) systems have been developed specifically for composites. The main difference between NDT and SHM is that the former can detect defects based on multiple inspection processes, increasing the time-holding for maintenance and overall running costs. To overcome these limitations, structural health monitoring systems are being implemented to continuously monitor the structure's integrity, reducing the costs and providing early stage detectability for defects development before failure [6].

Different sensors are used in SHM systems to monitor composite structures. Most common sensors are strain gauges [9], fibre Bragg grating sensors (FBGs) [10], and piezoelectric transducers used to establish either an elastic ultrasonic wave in-situ inspection method [11] or an acoustic emissions-based inspection method [12].

Piezoelectric transducers have proven reliable to detect some types of the defects (delamination), while have not been reliable in detecting other types of defects such as cracks [13–15]. Piezoelectric transducers are expensive, require bulky design, and in some circumstances high power [16, 17].

Strain gauges are widely used to monitor composite structures. The use of graphene as an active element to measure strain has attracted interest within the research community. Graphene-based sensors have been used in different applications like prosthetics [18–20] and monitoring systems for strain sensing application sand as a pressure sensor in health care applications [21–25]. Graphene has been adopted as a strain sensing element [26–28] due to its good physical properties.

Although graphene is known for its outstanding mechanical and electrical performance, strain sensors based on graphene and used in composite structures have not been the focus of research studies. Graphene was introduced initially as part of various nanomaterials to achieve strain sensing elements [29–35] but few attempts were made to develop a full graphene-based strain sensor applied in a composite structure.

This paper presents a strain sensing system based on graphene. The graphene was selected as the sensing material to investigate the capability of printing custom-designed sensors to monitor composite materials instead of the use of commercially available strain gauges. The novel sensor is used in composite structures for in-situ strain monitoring. It is expected that the sensor will be printed over large areas to minimise electrical connections while maintaining a high level of strain sensing for composite structures during service.

Different loading scenarios are examined: tensile loading, compression loading, linear and cyclic loading conditions. Commercially available strain gauges were used for benchmarking the graphene sensors performance. The graphene sensor is finally evaluated in terms of strain detectability and gauge factor.

2 Modelling

The operating principle of the graphene sensor is the change in the electric resistance value of a thin layer of graphene ink when a tensile or compression load is applied [27]. Graphene ink is a complex nanomaterial consisting of graphene flakes, a polymer binder, and a solvent [36, 37]. The electrical conductivity of the graphene layer is defined by the electrical conductivity and dielectric permittivity of the solid residue of the ink that comes in the form of conductive graphene flakes dispersed in a dielectric polymer binder matrix [38]. Additional intentional or unintentional solid inclusions inside the mixture and defects introduced during its application on a surface affect the final electrical conductivity of the ink.

Numerous publications have attempted to describe the mechanism of electrical conduction for percolating conductive particles in an insulating matrix [39]. Conductive

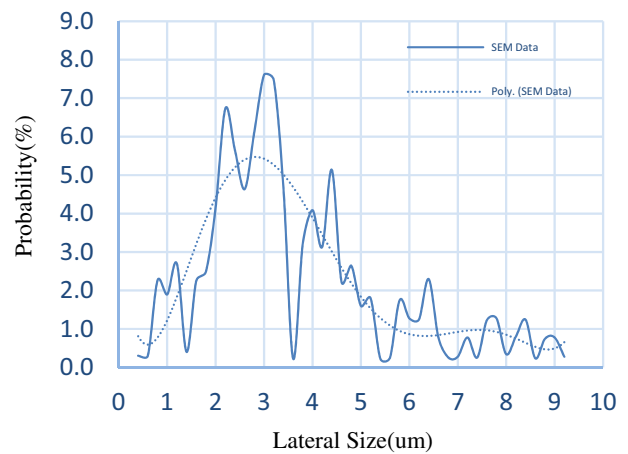


Fig. 1 The probability distribution functions are used to generate lateral size of the graphene flakes on the model (adapted from [41])

particles include nanowires, carbon black, carbon nanotubes or fullerenes and graphene flakes. Modelling has been used in that effort, though the complexity of such nanocomposite materials usually results in numerous approximations being introduced to the models [40]. To attain a qualitative understanding of the conduction mechanism for the graphene ink used for this work, a software suite for material characterization on a micro-scale was used [41]. With the use of this software (Math2Market GeodictTM), we generated percolating networks of graphene inks in a polymer matrix and solved for electrical conductivity to calculate the electric resistance, electric field, potential and current distribution when a unitary DC excitation is applied (1 Volt DC).

An accurate model of the specific type of graphene ink used for this work was generated using statistical data derived from the image processing of SEM images. Each flake was stochastically generated as a flat polyhedron using statistical distributions that describe its thickness and lateral size as shown in Fig. 1. The thickness of the flakes was determined by a Gaussian distribution. The flakes lateral size was generated with the use of a probability distribution function derived from previous work [36].

The graphene flakes were piled on top of each other and encased in a polymer matrix [42] matrix to create a rectangular, 1 um thick layer of graphene ink as shown in Fig. 2. The volume fraction of the flakes in the resulting film was 6.25% by weight [36]. A uniform distribution of the graphene flakes over the film's entire surface area has been assumed.

A voltage of 1 V was applied along the length of the rectangular sheet of graphene ink. The static electric current solver generated a visualization of the resulting electric field shown in Fig. 3. The electric field visualization shows

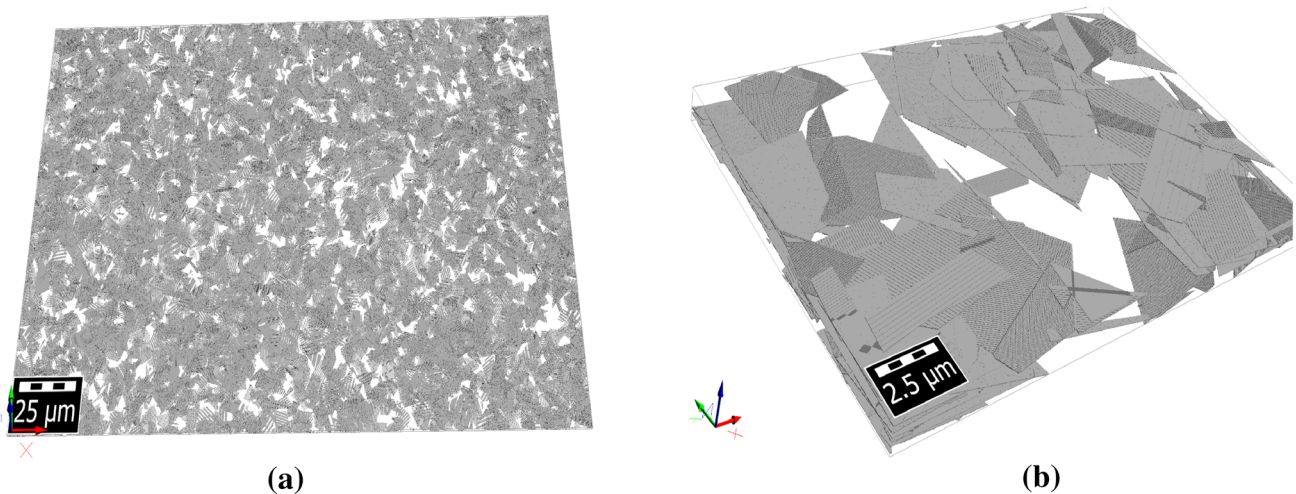


Fig. 2 Graphics rendering of the graphene ink model: **a** full scale, **b** detail

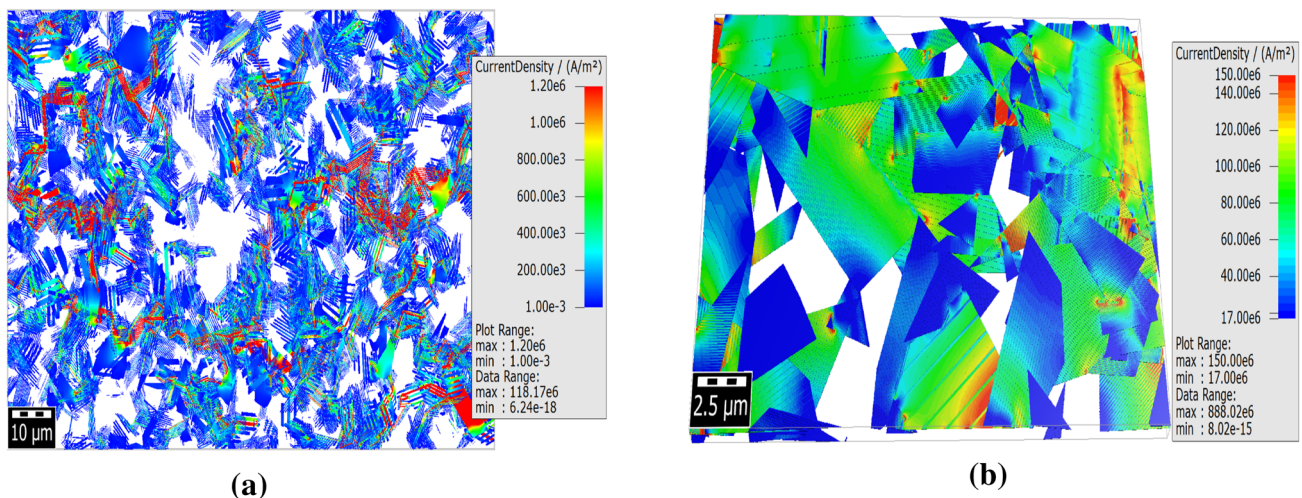


Fig. 3 Visualisation of the DC current distribution for the full-scale model **a** and a small detail **b**. Conduction paths are highlighted with red/yellow colour

the conductive paths and current distribution between adjacent, “contacting” flakes.

Multiple rectangular graphene sheets were generated and the resistance of each was derived from the simulation results. Due to the conduction path’s randomness, a significant standard deviation of more than 15% was calculated. This deviation is lowered with increasing surface area of the graphene ink layer, which results in multiple conduction paths existing simultaneously. This effect is demonstrated by the electric field and potential distributions, which become more homogeneous with increasing model size as seen in Figs. 4 and 5.

To further investigate the conduction mechanism on larger scale models of the graphene sensor, a Python script

was created and executed in conjunction with the API of CAD software to generate graphene flakes with the identical probability distributions as before for thickness and lateral size [36] and populate a significantly increased surface area. The only difference is that the shape of the graphene flakes in this case was approximated as a disk instead of a flat polyhedron, as presented in Fig. 6, to simplify the model geometry. The coordinates of each flake were modified to simulate the dilation and compression effects that take place within the graphene ink micro-structure during tensile and compressive tests respectively. The structure of the ink derived from Figs. 4, 5 and 6 showed that the structure undertakes a series of changes when subject to either a tensile load or a compressive load. The modelling

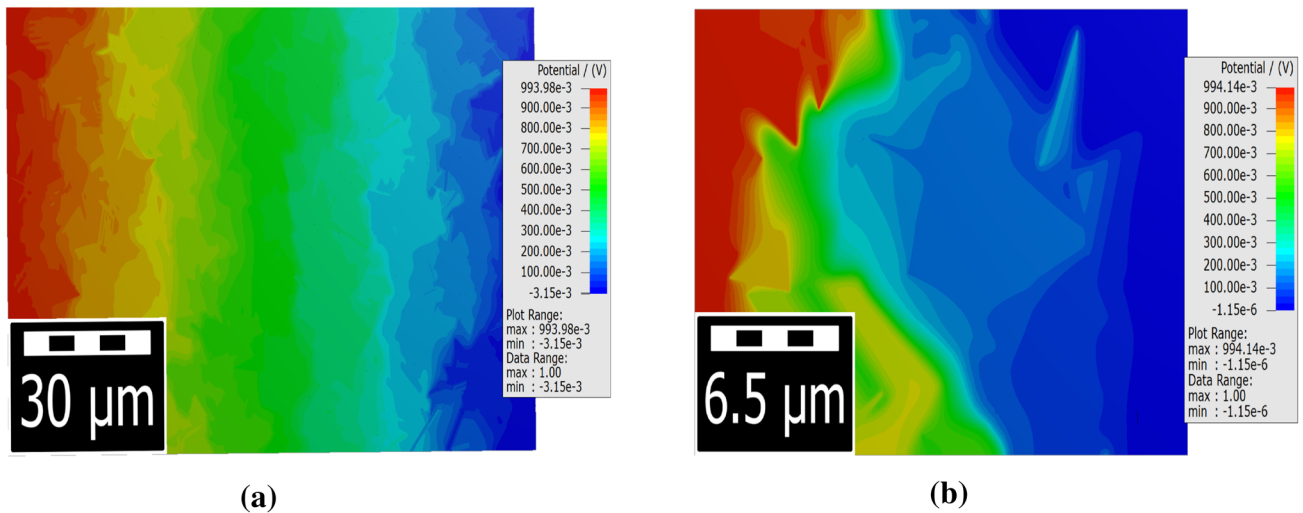


Fig. 4 Visualisation of the potential distribution for a full-scale **a** and a small detail **b** of a graphene ink layer

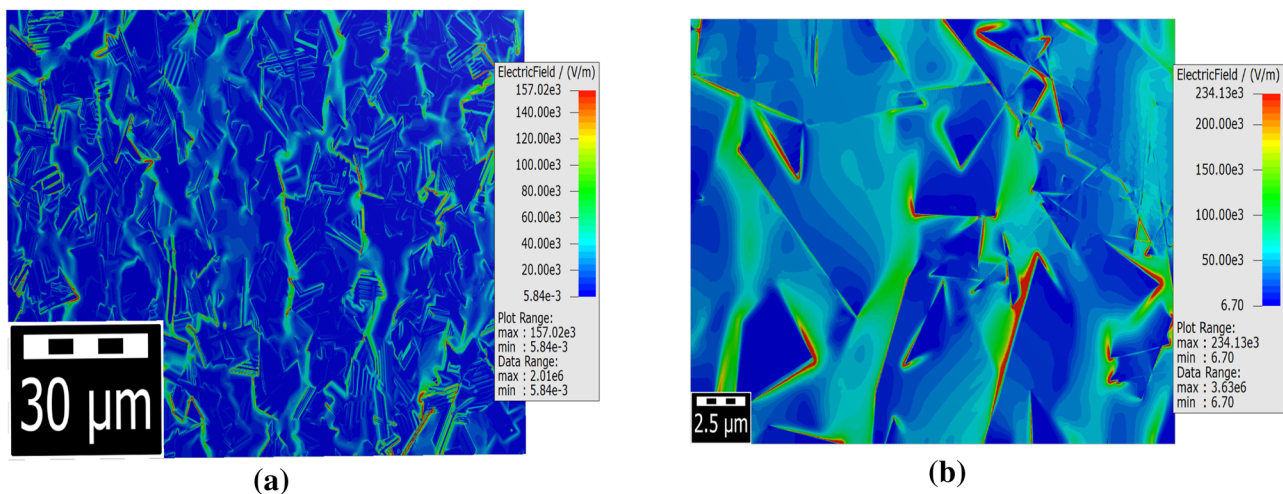


Fig. 5 Visualisation of the electrostatic field distribution for a full-scale **a** and a small detail **b** of a graphene ink layer

provided a model to understand these changes when the sensor is stretched and how it can measure the strain when attached to a structure.

An additional Python script was created utilizing the CAD software API to detect contact points between adjacent graphene flakes. The script produces a connectivity matrix, i.e., a graph that describes all the connections between graphene flakes in the model [43]. A uniform contact resistance approximation was used [40] that equates the contact resistance between any pair of interconnecting graphene flakes to an effective constant value. This approximation becomes less pronounced for largescale

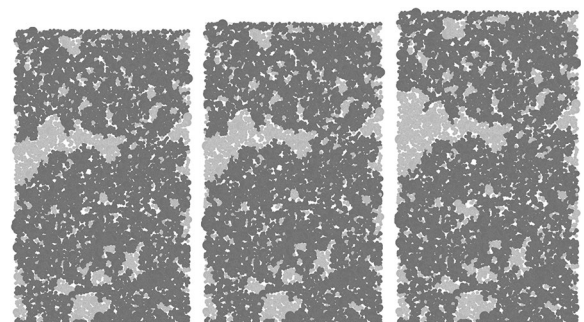


Fig. 6 Top view of a series of instances of a script-generated graphene ink model that correspond to different values of strain

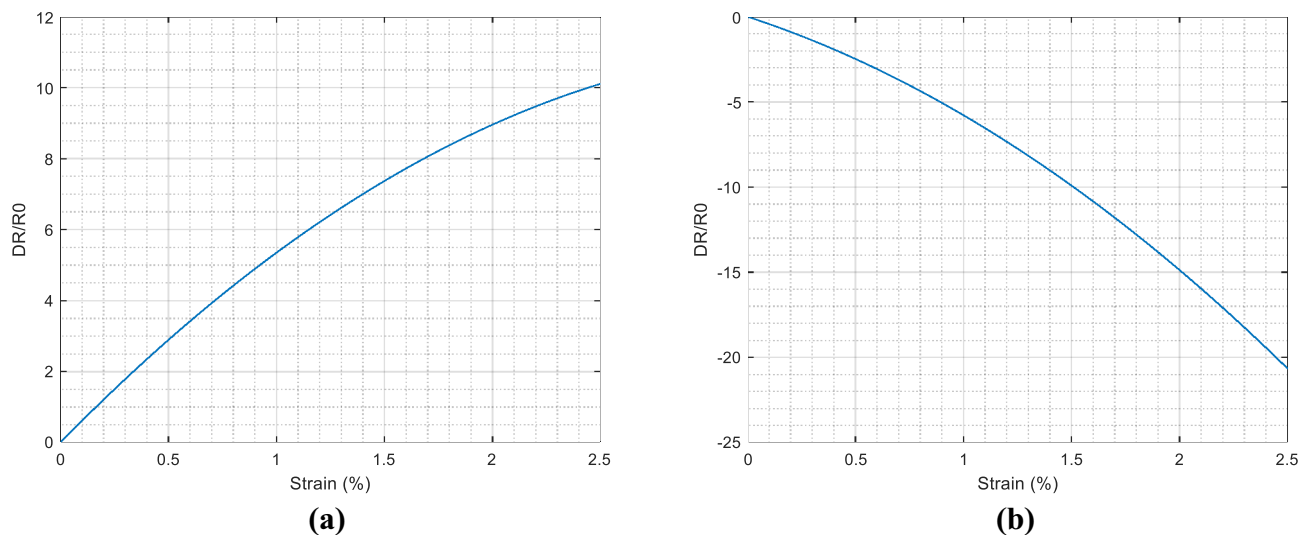


Fig. 7 DR/R0 in the function of strain obtained from the modelling for a graphene-based strain sensing element under tensile load **a** and compression loading **b**

models due to the existence of multiple conduction paths in parallel and it allows for the calculation of the resistance of a strip of graphene ink as a function of the effective constant resistance value. Multiple resistance values are thus computed, each corresponding to a strain value of the same sensor model. By calculating the ratio between the resistance delta of each instance delta to the reference (DR), no strain resistance value (R0), the effective contact resistance factor is expunged [44]. The sensitivity plots, shown in Fig. 7, were then plotted for the strain sensor.

3 Experimental setup

The sensor was manufactured using the graphene ink developed by DZP technologies (product reference G0240).

The graphene ink, designed as a percolative sensor, was printed on different substrates and attached to different composites coupons; an industrial-grade electrically enhanced carbon prepreg composite material (reference: Haydale GA-ELC [45]) and an industrial-grade quadaxial [0/−45/90/+45] E-glass composite material, both supplied by Haydale. The composite coupons were also provided by Haydale Ltd. Table 1 summarizes the different configurations for the graphene-based strain sensor and the substrate used as a base to attach such sensor to the testing samples.

Two different scenarios, shown in Fig. 8, were selected to perform the tests. In the first scenario we attached the graphene sensor on the surface of the composite coupon. On the edges, a silver conductive ink was printed for

connecting to the data logging system. The silver ink was used to maintain the electrical connection between the wires and the graphene sensor during all the experiments investigated in the paper. The graphene ink and the silver ink were printed on a substrate and then attached to the surface of the composite coupon. In the second scenario, the graphene sensor was embedded in the composite. It was placed between the two middle plies (Fig. 8).

For both scenarios, a data logging system was used to capture the voltage changes as load is applied to the composite coupon.

The graphene sensor was printed directly on the GFRP sample and on a PET transfer film on the CFRP coupons. This is due to the fact that the CFRP material's is conductive and the signal would be affected by attaching the graphene sensor directly to the surface of the sample.

Tensile and compression tests were performed on an Instron 250 kN 8802 Universal Test Machine (UTM). The UTM, shown in Fig. 8b was controlled by a computer which recorded time, displacement and the applied load. A strain gauge was attached at the centre of the opposite surface as to where the graphene sensor was attached. The strain gauge had a gauge factor of 2. The strain gauge signals were recorded using a National Instrument Strain Logging unit strain data logging system. The signals from the graphene sensor were logged using a customized system developed by ADVISE DETA.

Multiple scenarios, summarized in Table 2, were tested to investigate real-life scenarios and conditions.

Table 1 Sensor design scenarios

ID	Test	Material	Sensor location	Method of attachment
1.1	Tensile	CFRP	External surface	Acrylate adhesive (Loctite) with PET transfer film
1.2	Cyclic tensile	CFRP	External surface	Acrylate adhesive (Loctite) with PET transfer film
1.3	Compression	CFRP	External surface	Acrylate adhesive (Loctite) with PET transfer film
2.1.1	Tensile	GFRP	External surface	No transfer film is used
2.1.2		GFRP	Embedded sensor	
2.2	Cyclic tensile	GFRP	External surface	No transfer film is used
2.3.1	Compression	GFRP	External surface	No transfer film is used
2.3.2		GFRP	Embedded sensor	

Where:

T_CFRP: Tensile test (T) Carbon Fibre Reinforced Polymer (CFRP)

CT_CFRP: Cyclic Tensile test (CT) Carbon Fibre Reinforced Polymer (CFRP)

C_CFRP: Compression test (C) Carbon Fibre Reinforced Polymer (CFRP)

T_GFRP: Tensile test (T) Glass Fibre Reinforced Polymer (GFRP)

CT_GFRP: Cyclic Tensile test (CT) Glass Fibre Reinforced Polymer (GFRP)

C_GFRP: Compression test (C) Glass Fibre Reinforced Polymer (GFRP)

Fig. 8 Graphical illustration showing **a** the graphene sensor and strain gauges positions on the testing coupons: graphene sensor on the surface (left) and graphene sensor embedded within the composite structure (right) and **b** the experimental apparatus to evaluate the performance of the graphene-based strain sensing system

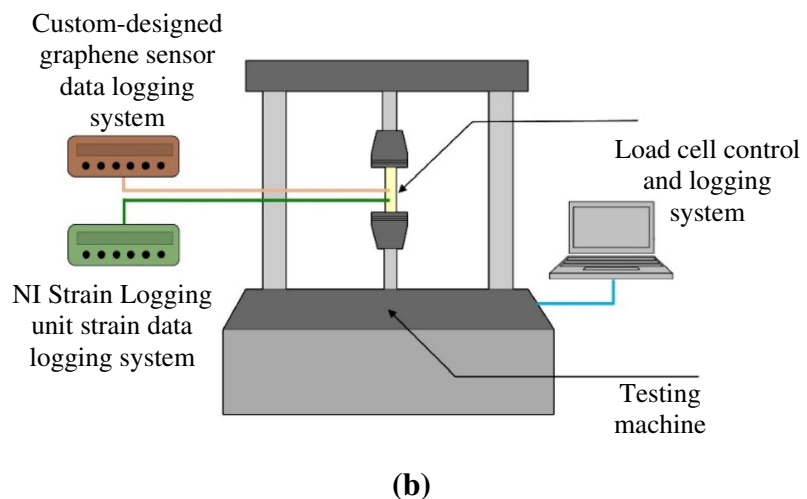
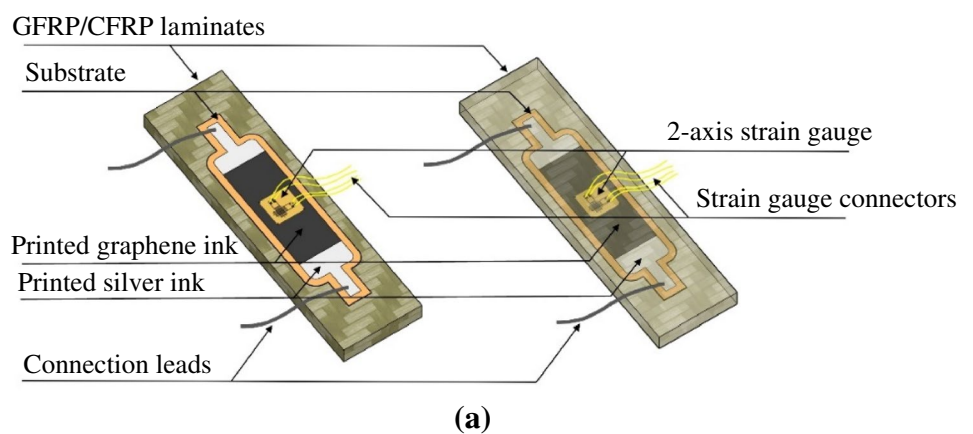


Table 2 Testing scenarios for the composite coupons

ID	Dimensions (mm)	Test type	Displacement rate (mm/min)
1.1	25×2.5×250	Tensile	1
1.2	25×2.5×250	Cyclic tensile 10 cycles	2
1.3	13×2.5×140	Compression	1
2.1.1	25×2.5×250	Tensile	1
2.1.2	25×2.5×250	Tensile	1
2.2	25×2.5×250	Cyclic tensile 10 cycles	2
2.3.1	13×2.5×140	Compression	1
2.3.2	13×2.5×140	Compression	1

4 Results

4.1 Graphene sensor attached on the surface of the structure

4.1.1 Sensor response under tensile loading

The first set of experiments consisted of applying a tensile load scenario with two different variants: normal tensile load and cyclic tensile load. The results of the strain measurements and the graphene sensor output voltage are presented in Fig. 9a-d. The graphene sensor is attached to the CFRP coupon surface as detailed in Sect. 3.

In the normal tensile load test, the voltage measured from the graphene sensor correlated with the results obtained by the strain gauge. Initially (up to about 60 s), the voltage increased linearly for both the graphene sensor and the strain gauge. The corresponding slopes are reported in Table 3.

After 60 s, both the strain gauge and the graphene sensor sensitivity to the applied load reduced. This resulted in lower slopes measured in the signals. Similar behaviour can be seen in the cyclic load results. More interesting features are revealed as the graphene sensors could detect the change in strain but the amplitude of the change is slightly varying but remains within $\pm 5\%$ range.

Figure 9e-f show the DR/R0 and the strain for both sets, the normal tensile load, and the cyclic tensile load. Similar to the voltage curve, the resistance of the graphene sensor increased when the applied strain is increased and the difference in resistance DR between the measured R and the initial sensor resistance R0 became minimal when a high level of strain is achieved. The DR/R0 showed in the Fig. eleven is showing a nonlinear behaviour while the strain measured from the commercial strain gauge is considered linear. This is due mainly to the measuring physics as the graphene sensor is based on percolation leading to changes in the resistance of the material when subject to an externally-applied strain.

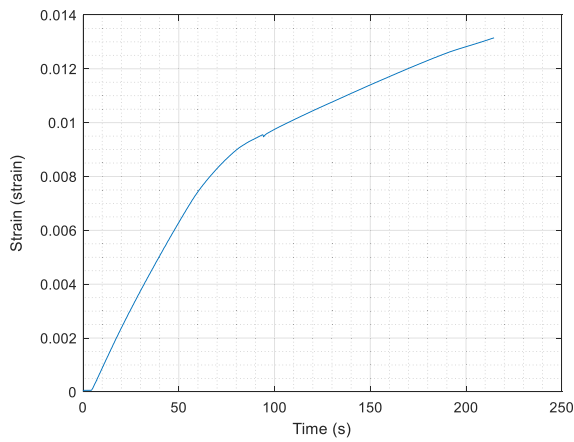
During the cyclic load, the resistance of the sensor varies under the strain applied. It can be noticed that the resistance variation is taking slightly longer to manifest. This is due to the material behaviour.

The results for the GFRP testing are summarized in Fig. 10a-e. Although the strain curve shows a linear pattern, the graphene voltage output displays a non-linear behaviour for the normal strain load. In the case of the cyclic load, the graphene sensor is showing promising results in measuring the strain generated as multiple tests showed a repeatability of $\pm 5\%$. The cyclic load results are showing that the graphene sensor can reasonably follow the trend of the strain generation by applying a tensile load.

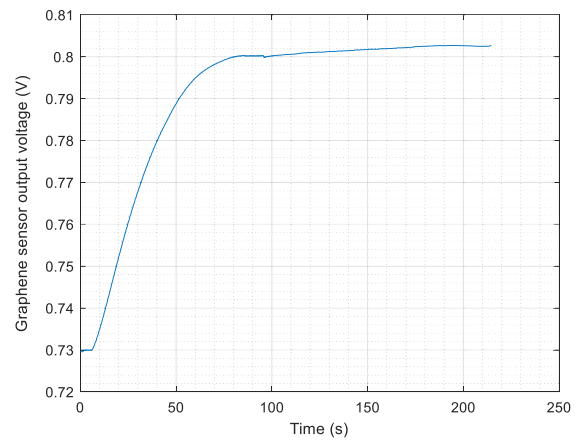
Figure 10e-f detail the DR/R0 variation of the graphene sensor when a load is applied. It can be seen that the internal resistance of the sensor is variable at a similar behaviour to the strain generated within the coupon. It is important to observe that the scale for both reading for the strain and the voltage output in Fig. 10 is different. Qualitatively, when the cyclic load is applied, the recorded amplitude from the strain gauge varies by $\pm 3.33\%$ while the graphene sensor recorded output is varying by $\pm 2\%$ offering a greater stability to measure rapid cyclic loads. The variation can also be explained by the fact that when using a commercial strain gauge, the strain is sensed through an attachment film while in the case of the graphene ink, the flakes were in direct contact to the main substrate which increases the complexity of the interaction between the composite sample and the ink. Further lab-based experiments showed that by increasing the time of the cyclic test, the graphene ink was able to regain its original configuration and provided a similar reading in the region where the strain is null.

It can also be noticed that there is a minimal offset time between the strain generated and the response of the sensor and similarly when the load is decreasing, the graphene sensor is taking slightly longer to respond. This effect is expected as the cycling test is relatively faster than the relaxation period of the sensor. Additional experiments showed that by increasing the cycle time, the results show perfect repeatability. The graphene sensor used to conduct these experiments contains a polymer binding material which is inducing the delay in response for the graphene sensor. The response recorded from the strain gauge shows a linear sensing profile but for the graphene sensor, the response curve to the applied strain displays a non-linear behaviour at the beginning and at the end of each cycle. This effect is similar to the relaxation effect as the material takes longer to establish the initial position when there is no strain applied.

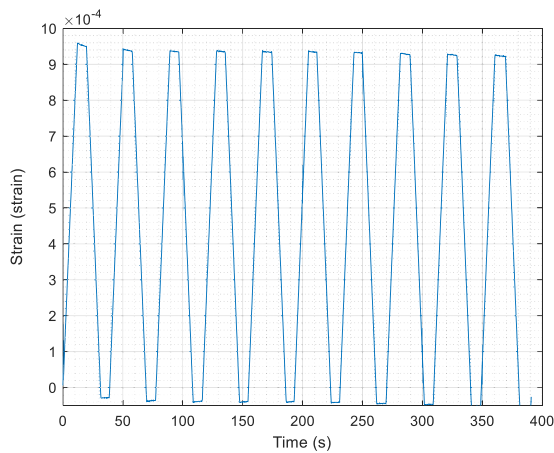
For both materials, CFRP and GFRP, the graphene sensor voltage output and the DR/R0 variation show similar



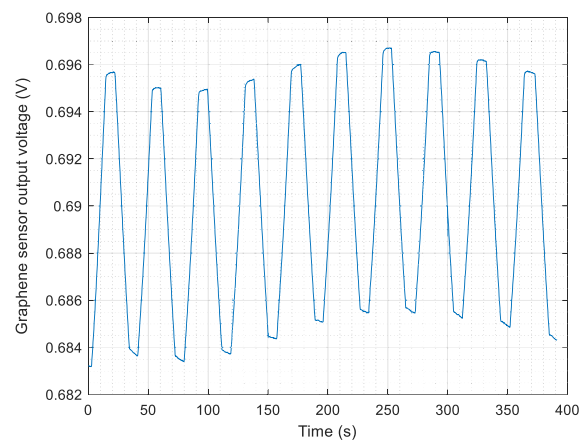
(a)



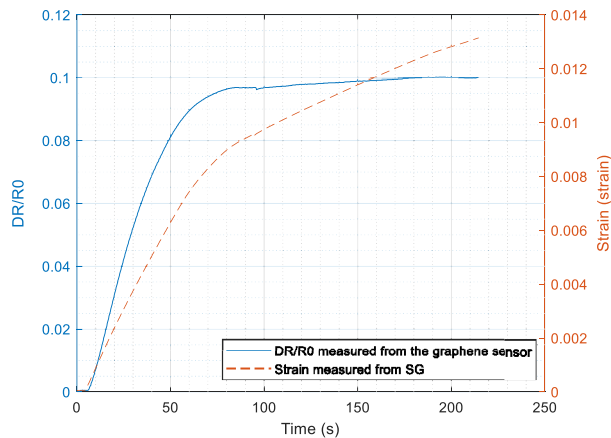
(b)



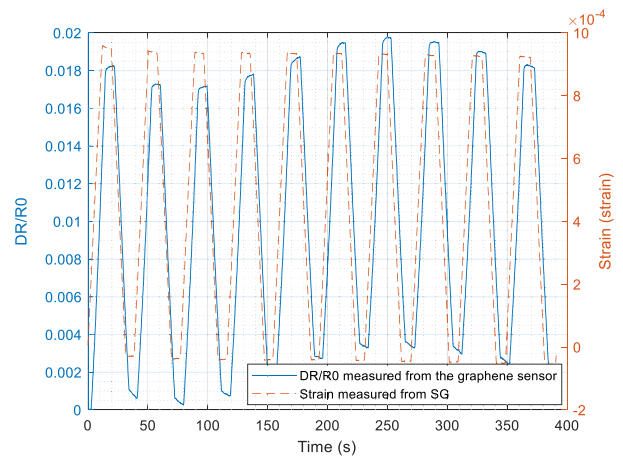
(c)



(d)



(e)



(f)

Fig. 9 Strain measurement obtained from strain gauge **a** and graphene sensor output voltage **b** for a normal tensile load applied to a CFRP sample and 10 cycles cyclic tensile load **c** and **d** respectively and resistance change comparison for the graphene-based strain

sensor to strain measurement obtained from strain gauge under **e** normal tensile load and **f** 10 cycles cyclic tensile load applied on a CFRP coupon

Table 3 Correlation between the signals from the graphene sensor and the strain gauge

Sensor	Slope from 0 to 60 s	Slope for $t > 60$ s
Graphene Sensor	1.11×10^{-3} V/s	4.0×10^{-5} V/s
Strain Gauge	1.22×10^{-4} strain/s	3.0×10^{-5} strain/s

patterns to the variation of the strain generated within the sample. The next set of experiments consists of applying a compression load, both normal and 10 cycles cyclic load to CFRP coupons and GFRP coupons.

4.1.2 Sensor response under compression loading

The results and key findings involving the characterization of the graphene sensor and the strain gauge within a CFRP sample subject to a compressive load are summarized in Fig. 11.

The results show that the graphene sensor provides a similar pattern and behaviour to the strain gauge. The response of the graphene to applied strain is fundamentally different to the response of copper-based strain gauges. The graphene sensor responds to strain through the percolation effect. The response of the material is non-linear when strain is applied leading to a non-linear trend for the sensor response to the applied strain as it is reported in [46]. Through modelling and calibration, the fluctuation in the signal can be corrected and compensated to reflect similar behaviour to the commercial strain gauges.

The DR/R0 curve displays a similar delay compared to previous testing but better conformity to the material's strain. It can also be noticed that the difference in resistance between the initial sensor resistance and the resistance measured during the test is relatively high, which manifests in a steeper curve for DR/R0 as shown in Fig. 11c.

The next batch in the test plan consists of applying a compression load to a GFRP sample. Similar to the tensile load scenario, the graphene sensor was directly printed and applied to the surface of the sample.

The curves presented in Fig. 12a and b show a better performance for the graphene sensor in sensing the compression load and the generated strain within the material compared to the strain gauge. The voltage output from the graphene sensor reflects an accordance to the compressive strain applied to the GFRP sample. This performance is also reflected in the DR/R0 data shown in Fig. 12c.

4.2 Graphene sensor embedded within the composite material structure

The third scenario tested and covered through this paper is by embedding the graphene sensor with the composite structure. The process covers only the GFRP material as for the CFRP, it was difficult to isolate the graphene sensor to the main structure without substantially affect the sensor performance. The sensor was printed within the plies of the GFRP coupons, and the entire system was subject to tensile test and compression test. The results for both tests are shown in Fig. 13.

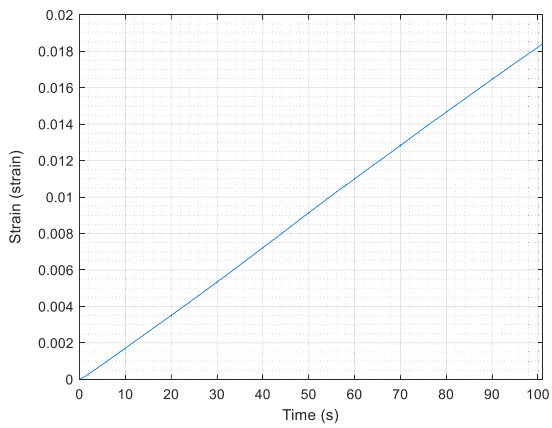
For the tensile tests, the graphene sensor response is non-linear compared to the linear increase of the measured strain. The graphene sensor response is lower when high strain levels are reached. Conversely, the graphene sensor's response during the compression test is similar to the strain measured by the strain gauge. This variation is reflected in the DR/R0 analysis shown in Fig. 14.

As seen in Fig. 14, the DR/R0 shows good conformity with the strain measurement curve. For the tensile load, the DR/R0 shows a non-linear behaviour which means that the graphene sensor sensing capabilities decrease for a high level of strain while showing a high sensing performance for lower strain levels. During the compression scenario, the graphene sensor was able to detect strain for relatively all ranges of strain with a slight delay at the beginning.

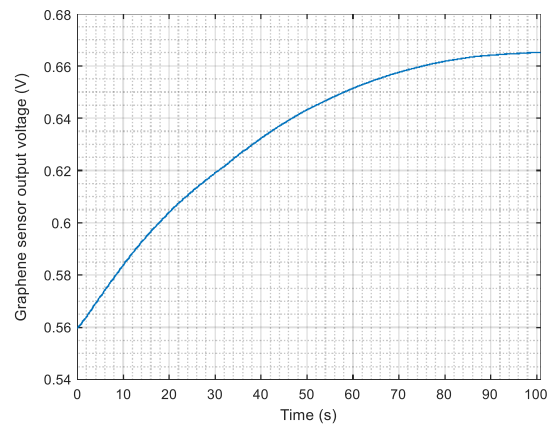
4.3 Gauge factor analysis

The work conducted focused on understanding the behaviour of the graphene-based strain sensor while printed either directly on the composite sample or attached to the coupons using a non-conductive substrate in the case of CFRP materials. Figure 15 shows the gauge factor calculated during the tensile testing for the CFRP material and GFRP material. As seen from both pictures, an interesting behaviour occurs as the gauge factor is not constant during the length of the testing and displays a non-linear trend.

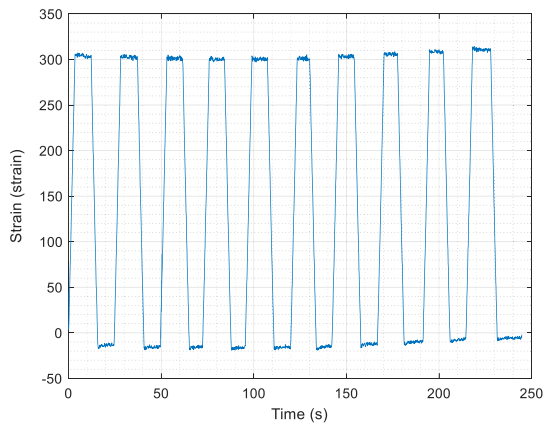
The curves show that the gauge factor is varying as a function of time. The gauge factor value's behaviour increases at the beginning of the test, corresponding to a low strain value reaching a global maximum around 2×10^{-3} for both CFRP and GFRP. After reaching the peak, the gauge factor starts decreasing with a stabilizing pattern at around gauge factor value equal to 6. The gauge factor for the graphene-based strain sensor is higher during the full test than the gauge factor from the commercial strain gauge.



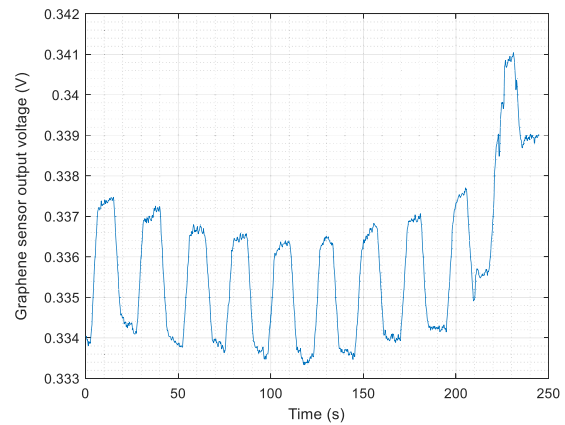
(a)



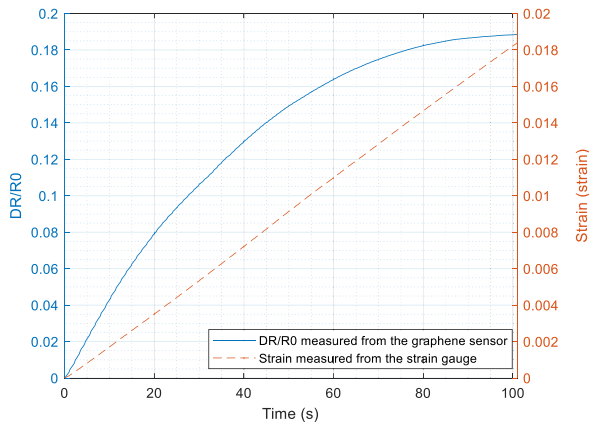
(b)



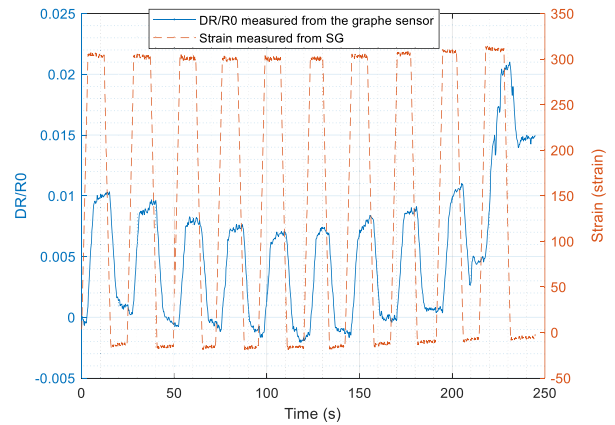
(c)



(d)



(e)



(f)

Fig. 10 Strain measurement obtained from a strain gauge **a** and graphene sensor output voltage **b** for a normal tensile load applied to a GFRP sample and 10 cycles cyclic tensile load **c** and **d**, respectively and resistance change comparison for the graphene-based

strain sensor to strain measurement obtained from strain gauge under **e** normal tensile load and **f** 10 cycles cyclic tensile load applied on a GFRP coupon

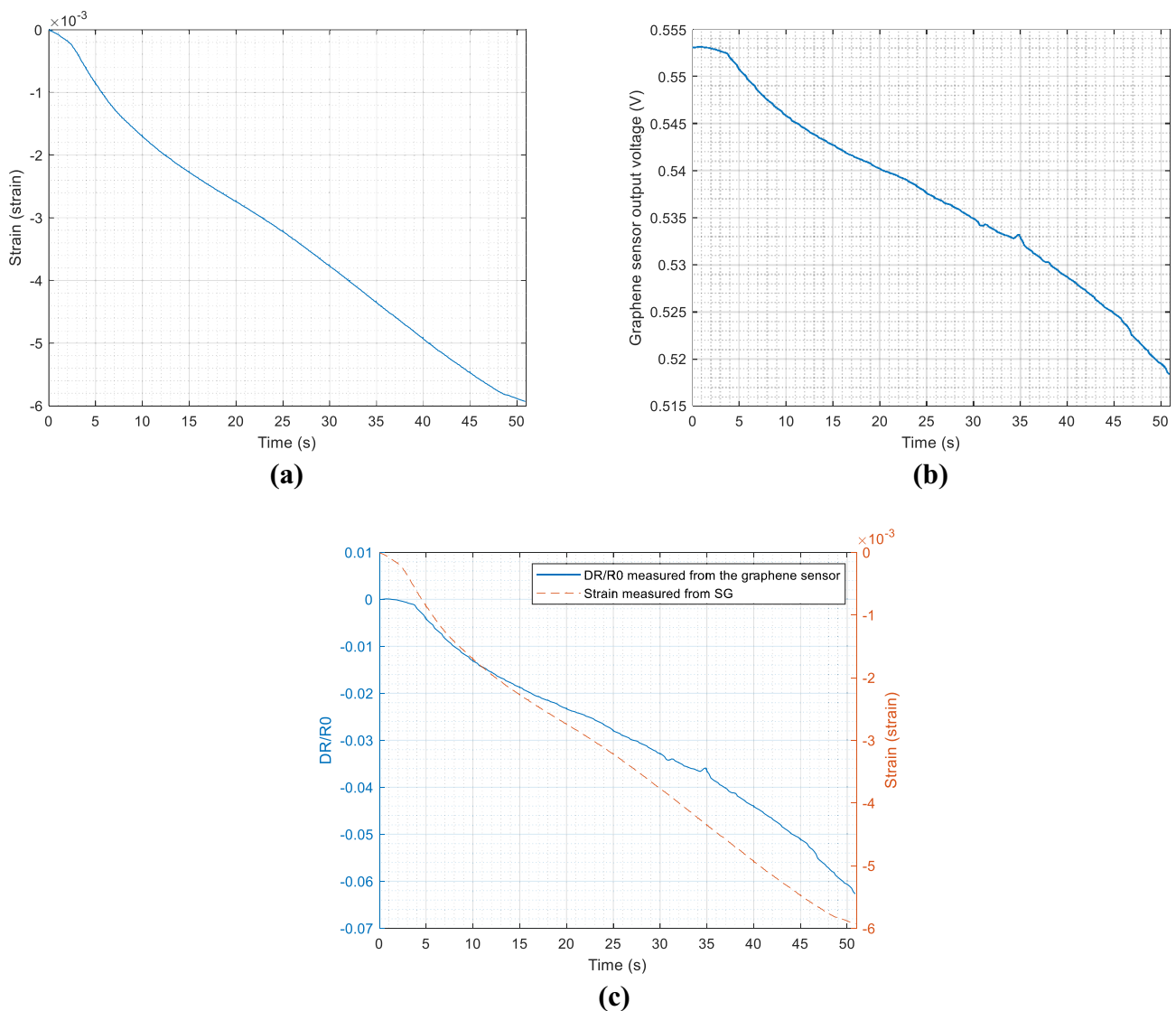


Fig. 11 Strain measurement obtained from a strain gauge **a** and graphene sensor output voltage **b** for a normal compression load applied to a CFRP sample and **c** resistance change comparison for

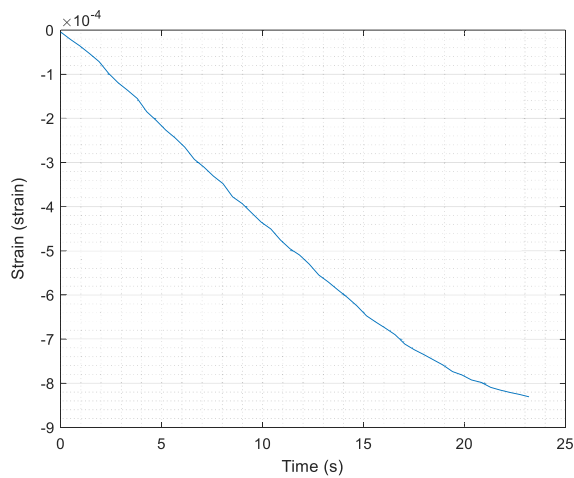
the graphene-based strain sensor to strain measurement obtained from strain gauge under normal compression load

5 Discussion

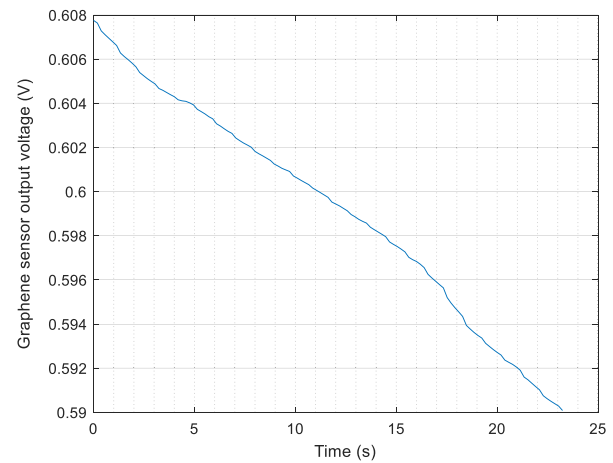
A graphene-based strain sensor was used to evaluate the strain generated within a composite sample. The tensile and compression results showed that the graphene could detect the strain similar to a commercial strain gauge. Interesting behaviour was seen for the tensile test as the graphene sensor provided a linear response for low strain values, but the behaviour became non-linear for higher strain levels. In fact, the graphene sensor was performing similar to the theoretical results obtained from the modelling. The ink response to strain was nonlinear which is expected as the ink was designed to perform as a percolation sensor. The nonlinearity of the results can

be controlled by modifying the chemical characteristics and the nanostructure of the printed sensor as it can be designed to behave as a dense material such as copper providing linear response to strain or designed to perform based on percolation theory leading to a nonlinear response to strain. The latter design would enhance the sensor sensitivity to strain changes compared to conventional design.

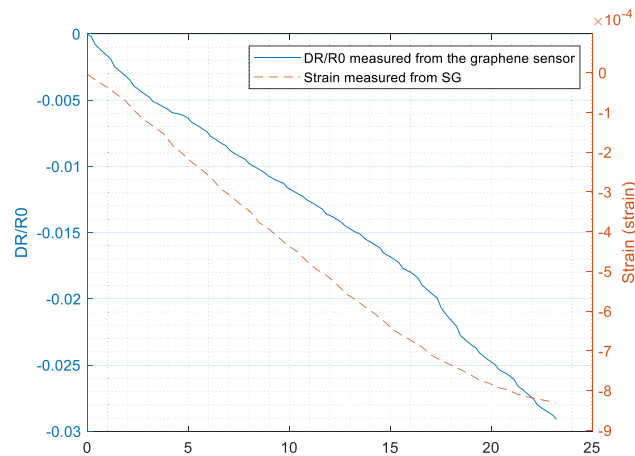
For the compression testing, the graphene sensor displayed good results in following the strain evolution trend. Conversely, the graphene sensor was able to detect the strain from the cyclic load and testing. The repeatability was challenging as the sensor exhibited a decrease in the overall amplitude. The amplitude of the signal generated



(a)



(b)



(c)

Fig. 12 train measurement obtained from a strain gauge **a** and graphene sensor output voltage **b** for a normal compression load applied to a GFRP sample and **c** Resistance change comparison for

the graphene-based strain sensor to strain measurement obtained from strain gauge under normal compression load

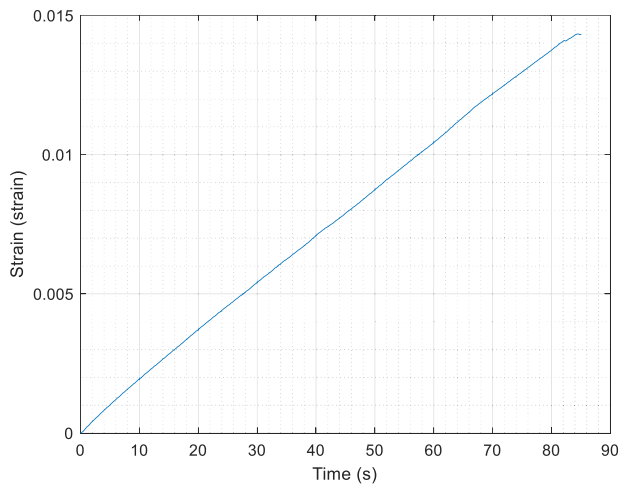
from the sensor was decaying while the number of cycles is increasing. This behaviour should be considered while designing the sensing system as the sensor exhibits a relaxation pattern.

The second batch of tests was conducted where the graphene sensor was embedded within the composite structure. This set of tests was conducted on the GFRP samples only. The graphene sensor was not printed on the CFRP because it is conductive and the results may be affected.

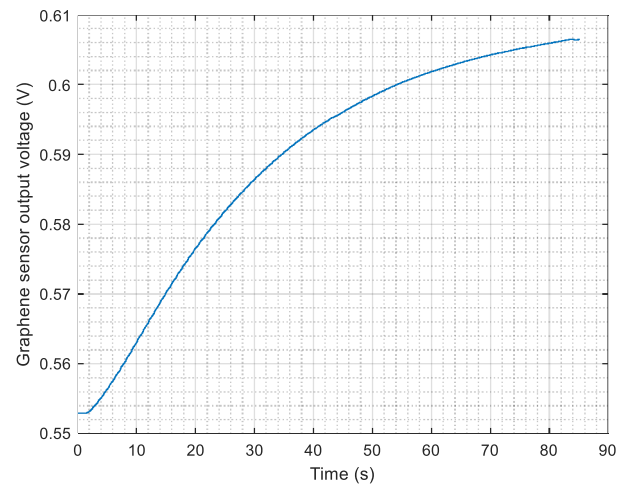
The overall analysis of the results showed that the sensor can detect strain within the composite structure. The gauge factor measured from the graphene sensor is higher than the commercial strain gauge sensors across the length of the testing.

6 Conclusions

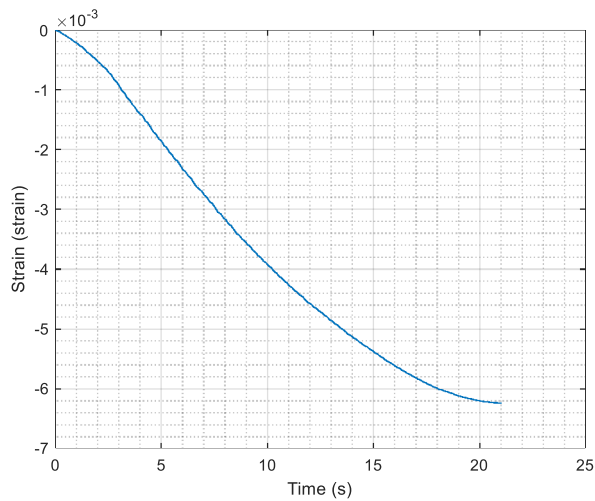
Composite structures are becoming widely used across different industries. Strain sensing is a critical task to assess and evaluate the health and the integrity of composite structure in-service. Conventionally, copper-based-commercially-available strain gauges were used. This type of strain gauges provided strain sense locally. Through the project, a new type of strain sensor was proposed. The new variation is based on graphene ink as the active element for strain sensing. Preliminary work showed that graphene-based strain sensors were able to detect deformation on and within composite coupons. The utilization of the sensor may present an alternative option and considered as a viable sensing element compared to the



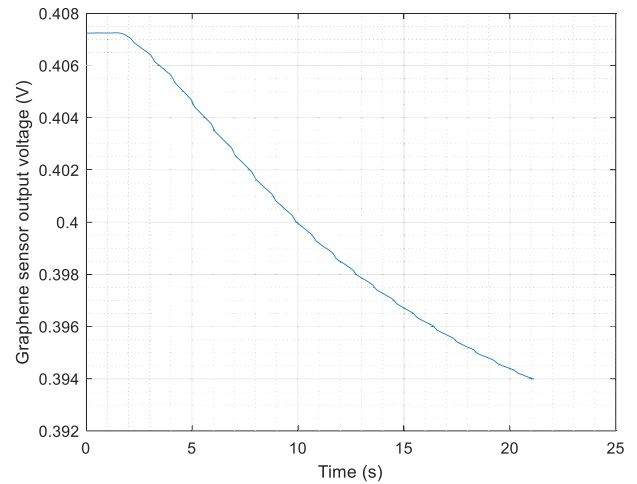
(a)



(b)



(c)



(b)

Fig. 13 Strain measurement obtained from a strain gauge **a** and graphene sensor output voltage **b** for a normal tensile load applied to a GFRP sample with embedded graphene sensor, and a normal

compression load applied to a GFRP sample with embedded graphene sensor **c** and **d** respectively

copper-based sensing systems currently used to evaluate the strain generated within the composite structure.

Different tests and scenarios were conducted to validate the sensor. The first batch of tests consisted of applying a graphene sensor on the surface of composite coupons and apply multiple load scenarios such as tensile, compression, 10 cycles tensile, and 10 cycles compression. Results showed that the graphene sensor could detect the strain levels with good agreement with results measured from the commercial system for both the tensile load and the compression load. Nonetheless, the use of a graphene sensor under cyclic loading is deemed challenging as the overall amplitude of the sensor’s output starts to decay while the number of cycles increases. Another observation

is that the sensor response presents a slight delay compared to when the load is applied. In fact, for the early cycles, the response of the sensor is perfectly matching the load profile; yet a slight delay is introduced for a higher number of cycles. Further investigation is needed to establish the effect of the number of cycles, and the length of each cycle on the response of the graphene sensor, as these details need to be taken into consideration when designing the sensor for in-situ monitoring in an industrial environment.

The second set of experiments consisted of embedding the sensor within the composite coupons. Preliminary results showed that the integrity of the structure is slightly affected, and this is majorly due to the wires connecting

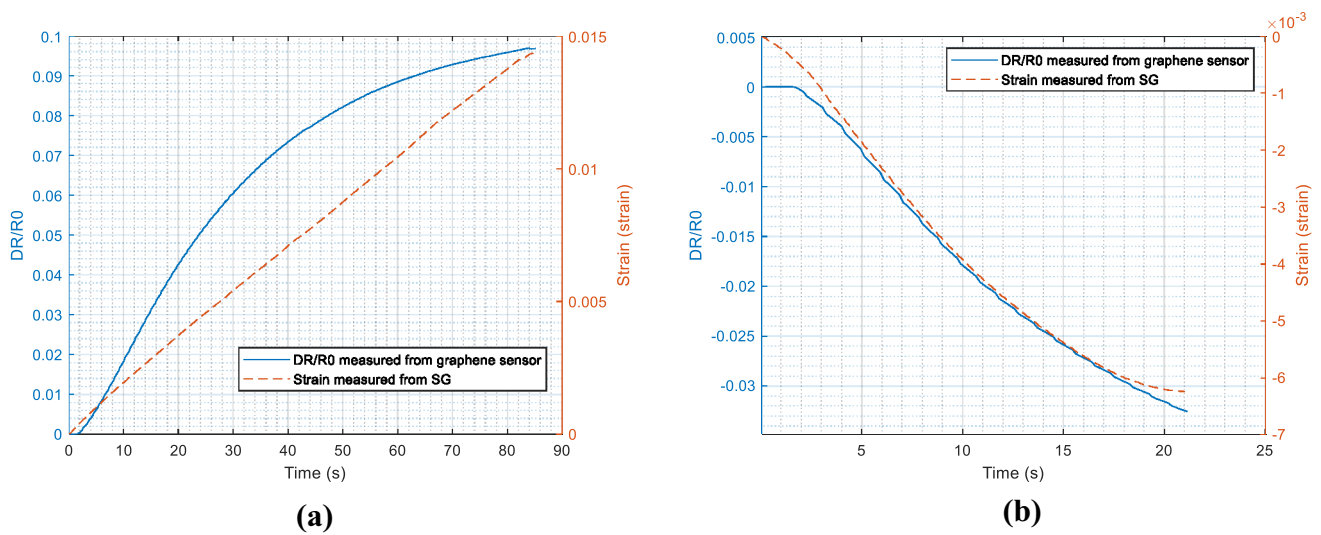


Fig. 14 Resistance change comparison for the graphene-based strain sensor to strain measurement obtained from strain gauge under **a** normal tensile load and **b** normal compression load applied on a GFRP coupon with an embedded graphene sensor for strain measurement

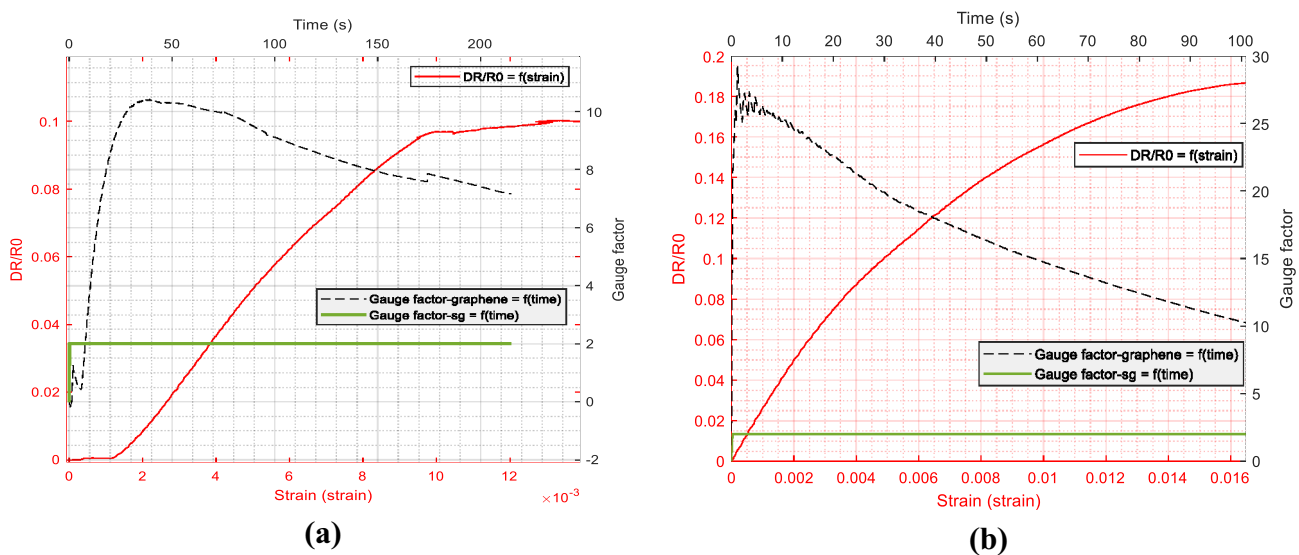


Fig. 15 Gauge factor variation the graphene-based strain sensor in the function of time calculated under normal tensile load for **a** CFRP sample and **b** GFRP sample

the sensor to the DAQ rather than the introduction of the sensor itself. The sensor was able to detect strain generated for both tensile load and compressive load. These tests were conducted using GFRP samples as the CFRP samples were conductive which would affect the measurement results.

Finally, the graphene sensor gauge factor analysis showed that the new proposed sensor is capable of assessing strain in different composite materials and samples while providing a higher gauge factor value compared to the commercial sensors. The graphene sensor can evaluate

strain with higher resolution compared to copper-based strain sensors. The graphene sensor used to monitor strain in different composite materials provided the capability of printing the sensor over large area for large specimen. Further work is being conducted to inspect large parts with industrial partners and results will be presented in future work. The sensor provided an easier process to inspect parts without the need for bulky experimental configurations and limited the need for multiple copper-based strain sensors which are needed to be attached to structures at multiple positions to provide insightful

information about generated strain within the inspected specimen. The different results presented as part of this work showed that the inspected part has minimal effect on the performance of the sensor. The main parameters that may effect the sensor are the percolation effect and the substrate material whether the sensor is directly printed on the structure or through a substrate. The proposed graphene sensor provided retrofittable capabilities as it can be attached to the surface of the structure as well as integrated within it during the manufacturing stage.

Acknowledgements The authors of the paper thank Haydale Ltd (Unit 10, Charnwood Business Park, North Road, Loughborough LE11 1QJ, UK) for providing the composite coupons and ADVISE DETA (34 Castle Rd., Bedford MK40 3PJ, UK) for developing and providing the logging system.

Author contributions Conceptualization, A.Z., and N.J.; Finite Element Modelling, D.F.; Formal analysis, A.Z, F.O and Z.S.; investigation, A.Z.; resources, Z.S and F.O.; writing—original draft preparation, A.Z.; writing—review and editing, A.Z, N.J and S.O.; supervision, M.K. All authors have read and agreed to the published version of the manuscript.”

Funding This work was supported by Innovate UK for the project GRAPHOSITE “A Graphene Sensor for Defect Detection and Predictive Maintenance in Composite Materials” [grant number 104266].

Declarations

Conflict of interest The authors declare no conflict of interest.

Consent for publication The authors hereby consents to publication of this article in SN Applied Sciences.

Open Access This article is licensed under a Creative Commons Attribution 4.0 International License, which permits use, sharing, adaptation, distribution and reproduction in any medium or format, as long as you give appropriate credit to the original author(s) and the source, provide a link to the Creative Commons licence, and indicate if changes were made. The images or other third party material in this article are included in the article’s Creative Commons licence, unless indicated otherwise in a credit line to the material. If material is not included in the article’s Creative Commons licence and your intended use is not permitted by statutory regulation or exceeds the permitted use, you will need to obtain permission directly from the copyright holder. To view a copy of this licence, visit <http://creativecommons.org/licenses/by/4.0/>.

References

1. Goossens S, De Pauw B, Geernaert T, Salmanpour MS, Khodaei ZS, Karachalios E, Saenz-Castillo D, Thienpont H, Berghmans F (2019) Aerospace-grade surface mounted optical fibre strain sensor for structural health monitoring on composite structures evaluated against in-flight conditions. *Smart Mater Struct* 28:065008
2. Jayasree N, Omairey S, Kazilas M (2020) Novel multi-zone self-heated composites tool for out-of-autoclave aerospace components manufacturing. *Sci Eng Compos Mater* 27:325–334
3. Vincent JDS, Rodrigues M, Leong Z, Morley NA (2020) Design and development of magnetostrictive actuators and sensors for structural health monitoring. *Sensors* 20:711
4. Carello M, Amirth N, Airale AG, Monti M, Romeo A (2017) Building block approach for structural analysis of thermoplastic composite components for automotive applications. *Appl Compos Mater* 24:1309–1320
5. Jayasree NA, Airale AG, Ferraris A, Messana A, Sisca L, Carello M (2017) Process analysis for structural optimisation of thermoplastic composite component using the building block approach. *Compos B Eng* 126:119–132
6. Clyne TW (2018) 4.7 thermal and electrical conduction in metal matrix composites. *Tech Rep* 4:188–212
7. Giurgiutiu V (2015) Damage and failure of aerospace composites. *Str Health Monit Aerosp Compos* 125–175
8. Garg AC (1988) Delamination—a damage mode in composite structures. *Eng Fract Mech* 29:557–584
9. Arena M, Viscardi M (2020) Strain state detection in composite structures: review and new challenges. *J Compos Sci* 4:60
10. Kahandawa GC, Epaarachchi J, Wang H, Lau KT (2012) Use of FBG sensors for SHM in aerospace structures. *Photonic Sens* 2:203–214
11. Towsyfyhan H, Biguri A, Boardman R, Blumensath T (2020) Successes and challenges in non-destructive testing of aircraft composite structures *Chin J Aeronautics* 33:771–791
12. Eaton M, May M, Featherston C, Holford K, Hallet S, Pullin R (2011) Characterisation of damage in composite structures using acoustic emission *J Phys Conf Series* 305:012086
13. Zhang J (2016) Defect detection, classification, and characterization using ultrasound. *Str Health Monit (SHM) Aerosp Compos* 307–323
14. Haile MA, Hall AJ, Yoo JH, Coatney MD, Myers OJ (2016) Detection of damage precursors with embedded magnetostrictive particles. *J Intell Mater Syst Struct* 27:1567–1576
15. Farrar CR, Lieven NA (2007) Damage prognosis: the future of structural health monitoring. *Philosophical Transactions R Soc Math Phys Eng Sci* 365:623–632
16. Zhou G, Sim LM (2002) Damage detection and assessment in fibre-reinforced composite structures with embedded fibre optic sensors-review. *Smart Mater Struct* 11:925
17. Kessler SS (2002) Piezoelectric-based in-situ damage detection of composite materials for structural health monitoring systems. *Massachusetts Inst Technol*
18. Kim J, Lee M, Shim HJ, Ghaffari R, Cho HR, Son D, Jung YH, Soh M, Choi C, Jung S (2014) Stretchable silicon nanoribbon electronics for skin prosthesis. *Nat Commun* 5:1–11
19. Lim S, Son D, Kim J, Lee YB, Song J, Choi S, Lee DJ, Kim JH, Lee M, Hyeon T (2015) Transparent and stretchable interactive human machine interface based on patterned graphene heterostructures. *Adv Func Mater* 25:375–383
20. Choi S, Lee H, Ghaffari R, Hyeon T, Kim D (2016) Recent advances in flexible and stretchable bio-electronic devices integrated with nanomaterials. *Adv Mater* 28:4203–4218
21. Yamada T, Hayamizu Y, Yamamoto Y, Yomogida Y, Izadi-Najafabadi A, Futaba DN, Hata K (2011) A stretchable carbon nanotube strain sensor for human-motion detection. *Nat Nanotechnol* 6:296
22. Liao X, Liao Q, Yan X, Liang Q, Si H, Li M, Wu H, Cao S, Zhang Y (2015) Flexible and highly sensitive strain sensors fabricated by pencil drawn for wearable monitor. *Adv Func Mater* 25:2395–2401

23. Pang C, Lee G, Kim T, Kim SM, Kim HN, Ahn S, Suh K (2012) A flexible and highly sensitive strain-gauge sensor using reversible interlocking of nanofibres. *Nat Mater* 11:795–801
24. Zang Y, Zhang F, Di C, Zhu D (2015) Advances of flexible pressure sensors toward artificial intelligence and health care applications. *Mater Horiz* 2:140–156
25. Chen S, Wei Y, Yuan X, Lin Y, Liu L (2016) A highly stretchable strain sensor based on a graphene/silver nanoparticle synergic conductive network and a sandwich structure. *J Mater Chem C* 4:4304–4311
26. Zha J, Zhang B, Li RK, Dang Z (2016) High-performance strain sensors based on functionalized graphene nanoplates for damage monitoring. *Compos Sci Technol* 123:32–38
27. Chun S, Choi Y, Park W (2017) All-graphene strain sensor on soft substrate. *Carbon* 116:753–759
28. Sebastian J, Schehl N, Bouchard M, Boehle M, Li L, Lagounov A, Lafdi K (2014) Health monitoring of structural composites with embedded carbon nanotube coated glass fiber sensors. *Carbon* 66:191–200
29. Liu Q, Gao R, Tam VW, Li W, Xiao J (2018) Strain monitoring for a bending concrete beam by using piezoresistive cement-based sensors. *Construct Build Mater* 167:338–347
30. Tseng S-F, Liao C-H, Hsiao W-T, Chang T-L (2021) Ultra-fast laser direct writing of screen-printed graphene-based strain electrodes for sensing glass deformation. *Ceram Int* 47(20):29099–29108
31. Chen Q, Sun Y, Wang Y, Cheng H, Wang Q (2013) ZnO nanowires–polyimide nanocomposite piezoresistive strain sensor. *Sens Actuators A* 190:161–167
32. Tadakaluru S, Thongsuwan W, Singjai P (2014) Stretchable and flexible high-strain sensors made using carbon nanotubes and graphite films on natural rubber. *Sensors* 14:868–876
33. Jeong YR, Park H, Jin SW, Hong SY, Lee S, Ha JS (2015) Highly stretchable and sensitive strain sensors using fragmented graphene foam. *Adv Func Mater* 25:4228–4236
34. Yan C, Wang J, Kang W, Cui M, Wang X, Foo CY, Chee KJ, Lee PS (2014) Highly stretchable piezoresistive graphene–nanocellulose nanopaper for strain sensors. *Adv Mater* 26:2022–2027
35. Trung TQ, Tien NT, Kim D, Jang M, Yoon OJ, Lee N (2014) A flexible reduced graphene oxide field-effect transistor for ultrasensitive strain sensing. *Adv Func Mater* 24:117–124
36. Brennan B, Spencer SJ, Belsey NA, Faris T, Cronin H, Silva SRP, Sainsbury T, Gilmore IS, Stoeva Z, Pollard AJ (2017) Structural, chemical and electrical characterisation of conductive graphene-polymer composite films. *Appl Surf Sci* 403:403–412
37. Banerjee I, Faris T, Stoeva Z, Harris PG, Chen J, Sharma AK, Ray AK (2016) Graphene films printable on flexible substrates for sensor applications. *2D Materials*. 4:015036
38. Park J, Kim KT, Oh DY, Jin D, Kim D, Jung YS, Lee YM (2020) Digital twin-driven all-solid-state battery: unraveling the physical and electrochemical behaviors. *Adv Energy Mater* 10:2001563
39. García-Macías E, Castro-Triguero R, Sáez A, Ubertini F (2018) 3D mixed micromechanics-FEM modelling of piezoresistive carbon nanotube smart concrete. *Comput Methods Appl Mech Eng* 340:396–423
40. Mutiso RM, Sherrott MC, Rathmell AR, Wiley BJ, Winey KI (2013) Integrating simulations and experiments to predict sheet resistance and optical transmittance in nanowire films for transparent conductors. *ACS Nano* 7:7654–7663
41. Uhlířová T, Pabst W (2019) Conductivity and Young's modulus of porous metamaterials based on Gibson-Ashby cells. *Scr Mater* 159:1–4
42. Biswas B, Chakraborty AK, Majumder M, Chowdhury A, Sanjal MK, Mallik B (2012) Surface electrical conductivity of poly (methyl methacrylate) thin films: observation of conductivity switching. *Synth Met* 161:2632–2637
43. Dimo P (1975) Nodal analysis of power systems. Editura Academiei Republicii Socialiste România
44. Sam S (2018) Integrating experiments and simulations in field-assisted nanowire chaining for high performance transparent electrodes, 11th International Symposium on Flexible Organic Electronics, Greece, 2–5
45. Haydale Graphene Industries, “Electrically Enhanced Prepreg,” material datasheet Nov 2019 [Revised v5]
46. Marsden AJ, Papageorgiou DG, Vallés C, Liscio A, Palermo V, Bissett MA, Young RJ, Kinloch IA (2018) Electrical percolation in graphene–polymer composites. *2D Mater* 5:032003

Publisher's Note Springer Nature remains neutral with regard to jurisdictional claims in published maps and institutional affiliations.